Film formation and surface renewal on a rotating spoked disk for polymer devolatilization

Junhao Wang [a, b], Hao Fu [a, b], Haibing Ding [c], Yufeng Qian [c], Zhipeng Li [a, b, *], Zhengming Gao [a, b, *], J.J. Derksen [d]

[a] Beijing Advanced Innovation Center for Soft Matter Science and Engineering, Beijing University of Chemical Technology, Beijing 100029, China

[b] State Key Laboratory of Chemical Resource Engineering, School of Chemical Engineering, Beijing University of Chemical Technology, Beijing 100029, China

[c] China Kunlun Contracting & Engineering Corporation, Beijing 100037, China

[d] School of Engineering, University of Aberdeen, Aberdeen AB24 3UE, UK

* Corresponding author. Tel.: +8610 64418267; fax: +8610 64449862. E-mail address: lizp@mail.buct.edu.cn (Zhipeng Li), gaozm@mail.buct.edu.cn (Zhengming Gao).

Highlights

- Film formation was studied using experiments, simulations, and dimensional analyses
- Circulations caused by the competition of gravity and viscous forces were analyzed
- Surface renewal rate of super-high-viscosity liquid decreases with increasing viscosity
- The scraper can limit the film thickness and increase surface renewal rate

ABSTRACT

The film flow and surface renewal of highly viscous liquid on a rotating spoked disk were investigated experimentally and numerically. In practical applications, the liquid is a polycarbonate melt with very high viscosity and Newtonian behavior at low shear rates. In the experiments, a maltose solution was used. The film thickness on the rotating disk was measured by an electrical conductivity probe. The Volume of Fluid (VOF) model combined with the sliding mesh method was used to simulate the film formation process. The simulated dimensionless film thickness and the film formation process agree well with the experimental results. The film flow and surface renewal under different operation conditions were evaluated. Gravity and viscous forces dominate the process with inertia playing a marginal role. A scraper was designed to intensify transfer processes on the film significantly.

Keyword: Devolatilization; Computational fluid dynamics; Highly viscous liquid; Film formation; Surface renewal

Nomenclature

A	Surface area [m^2]
D	Disk diameter [m]
$\boldsymbol{F}$	Additional body force [N]
$\boldsymbol{g}$	Gravitational acceleration [m^2/s]

H	Liquid height inside the reactor [m]
h	Disk thickness [m]
N	Disk rotating speed [rpm]
$\boldsymbol{n}$	Unit normal vector [-]
p	Pressure [Pa]
r	Radial coordinate [m]
S	Rate of film deformation [1/s]
T	Reactor diameter [m]
t	Flow time [s]
u	Velocity in x direction [m/s]
$\boldsymbol{v}$	Fluid velocity vector [m/s]
v	Velocity in y direction [m/s]
v_{tip}	Tip speed of the disk, $v_{\text{tip}} = \pi ND/60$ [m/s]
w	Velocity in z direction [m/s]

Greek letters

α	Volume fraction [-]
δ	Film thickness [m]
η	minimum distance between disk and wall or scraper [m]
θ	Angular coordinate [°]
κ	Curvature of the interface [-]
μ	Viscosity [Pa·s]
ρ	Density [kg/m^3]

Subscripts

g	Gas
l	Liquid

1 Introduction

Polycarbonate (PC) is one of the most widely used engineering plastics, with outstanding properties, such as impact resistance, electrical insulation, heat resistance, and optical transparency (Ganguly et al., 2021). During the process of PC synthesis, small molecular byproducts including phenol and water are produced. The byproducts must be removed in the last polycondensation stage to ensure the positive progress of the reaction and to obtain high-quality plastics with extremely few impurities. The techniques and equipment for intensifying polymer devolatilization have attracted a lot of interest (Sebastian and Biesenberger, 1983). The screw extruder has the characteristics of high shear and narrow residence time distribution and performs mixing and devolatilization at the same time (Coughlin and Canevari, 1969). The kneader has a large free volume and self-cleaning characteristics, and the increase in the cross-sectional area reduces the possibility of clogging (Palmer, 2000; Uwe Stueven et al., 2011). The horizontal disk reactor with a large specific surface area is a typical device in the polyester industry (Finkeldei, 2003; Kurt Hanimann and Werner Stibal, 2013). In a disk reactor a vertically oriented disk that rotates around a horizontal axis is partly immersed in a liquid bath. As a result of the rotation and viscous forces a liquid film forms on the

surface of the disk. The film is pulled down by gravity. The formation of the film on the surface of the disk increases the gas-liquid mass transfer area, and the renewal of the film also enhances the gas-liquid mass transfer process.

Film flows have been studied experimentally for a long time. Vijayraghvan and Gupta studied the film flow on a solid disk (Vijayraghvan and Gupta, 1982). They demonstrated that the measurement of film thickness by a pointed probe was quite accurate and presented an expression to calculate film thickness for low viscosity at high rotating speeds. Cheong and Choi (1995) conducted experiments to measure the molten polyethylene terephthalate (PET) layer thickness on a vertically rotating solid disk by using an electrical conductivity probe. Their results indicate that the rotational speed and gravitational force play an important role in determining the film thickness and shape for the polymer melt. Dwyer-Joyce et al. (2003) developed ultrasound as a method to determine the thickness of lubricating films in bearing systems. A laser scanning method also was applied to show the film on a solid disk (Miah et al., 2016). In the industrial production process, the viscosity of the PC material in the disk reactor is often greater than 500 Pa·s (super-high-viscosity) at about 200 □ (Ganguly et al., 2021), but the process of super-high-viscosity polymer devolatilization has not been rigorously investigated yet.

Computational fluid dynamics (CFD) plays an important role in studying the film formation processes on the disk. Afanasiev et al. (2008) investigated the influence of factors such as immersion depth and angular velocity on the thin film dynamics for a vertically oriented rotating solid disk partially immersed in a liquid bath with a finite element scheme. Hasan and Naser (2009) discussed the liquid film thickness on a rotating drum under laminar conditions by numerical investigations. They found that there was no steady-state solution to the film formation, because the dynamics are not stationary. Miah et al. performed numerical investigations of the film thickness distribution on a vertically rotating solid disk and hollow disks (Miah et al., 2016; Miah et al., 2017). The film thickness variations of hollow disks were lower than that of a solid disk, which reduces mass transfer resistance. A correlation equation was developed to describe the film thickness on the solid disk. Hu et al. investigated the hydrodynamics and mass transfer of the film on a vertically-aligned plate with an open window by means of CFD simulation (Hu et al., 2016, 2017). Results showed that the average film thickness of the confined free film in the open window region was about 0.50–0.67 of that in the solid region, while the film velocity was approximately 1.7–2.0 times higher. The liquid side mass transfer coefficient K_L of the confined free film was about 19% higher than that of the wall-bounded film. Xie et al. (2018) found that film flow behavior on a vertical plate with an open window was significantly different from that on an unperforated plate. The film had stronger vorticity due to the free surface inside the open window for low viscosity fluids.

Few studies have focused on film flow on a rotating disk with a spatula, where free film and scraped films can coexist. Cheng et al. studied the film formation characteristics within a horizontal twin-shaft disk reactor with an overlapping zone (Cheng et al., 2017, 2018). They studied syrup solutions with viscosities ranging from 4.4 to 68 Pa·s. It was confirmed that the scraped film is much thinner and more uniform than the free film for highly viscous liquids, which means that the mass transfer resistance can be greatly reduced. They also proposed that the reinforcement of film flow and surface renewal by the open window on solid disk decreases with increasing viscosity.

The aim of this paper is in the first place to explore the film formation of super-high-viscosity liquid on a vertical rotating spoked disk. In the second place, by comparing simulated dimensionless

film thickness with the experimental data, we validated our simulation results and numerical method. In the third place, based on the verified simulation methods and models, we investigated the operation condition and structure design to intensify transfer processes for polymer devolatilization.

The paper is organized as follows: in the next section, the experimental setup is discussed, including the rationale for the experimental material and film thickness measurement system. After that, the numerical approaches we used in this research are briefly summarized with references to the literature. In the subsequent results section, we first present the film formation characteristic of highly viscous liquid with the results of simulations and experiments. Secondly, we study the simulated film flow and surface renewal under different operating conditions, which help us to identify methods to intensify heat and mass transfer processes for agitation devices used for polymer devolatilization. Thirdly, we add a spatula to enhance the devolatilization process. The final section summarizes the main conclusions and suggests future directions.

2 Experiment

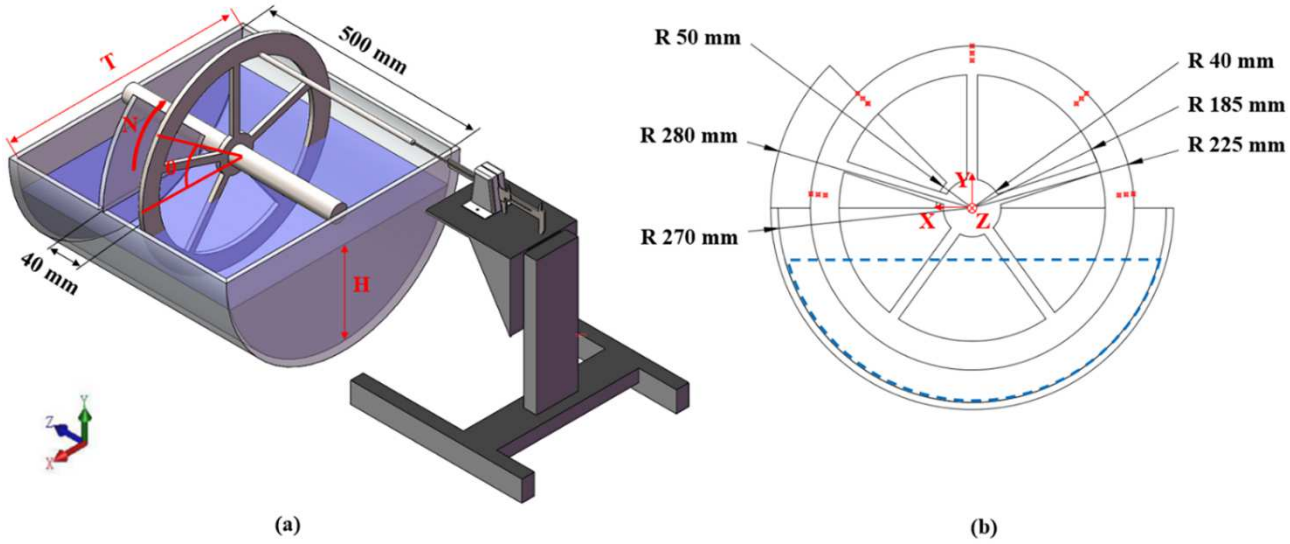

Fig. 1 - (a) Three dimensional reactor model and film thickness measurement system. (b) Section view. The cartesian coordinate system is located at the center of the disk. *T* is reactor diameter, *H* is liquid height inside the reactor, *N* is disk rotating speed, and *θ* is angular coordinate, which is not moving with the wheel. The fluid region is shown in blue. The red points in panel (b) are the measurement positions of the electrical conductance probe.

Fig. 1(a) shows the experimental setup including a vertical rotating spoked disk reactor device. The reactor is made of Polymethyl methacrylate (PMMA). The stainless-steel spoked disk includes five open windows and five spokes, shown in Fig. 1(b). The diameters of the reactor, disk, and shaft are 540 mm, 450 mm, and 40 mm, respectively. The thickness of the disk and scraper is h=10 mm. The location of the scraper can be adjusted or it can be removed.

As shown in Fig .1(a), the film thickness measurement system includes a three-dimensional positioning system, a micrometer (ASIMETO), and an electrical conductance probe. When the probe touches the surface of the film or metal disk, the electric current changes. The distance

between the film surface and the disk is seen as the film thickness on the disk, which is measured by the micrometer. The probe and micrometer are located on the three-dimensional positioning system, which move accurately to the measurement position specified. The probe cannot measure in the open windows when the disk is running. Thus, only the film thickness on the solid disk is measured if the radial coordinate is between 185 mm and 225 mm, see Fig. 1(b). The film thickness measurements for each point are performed five times and the average value is recorded.

A rationale for experimental materials selection is necessary. The operating speed of the industrial PC production process is low. The speed of this experiment is consistent with the industrial process. The operating speed of the PC production process in industry is low. We estimate the maximum shear rate on the disk through the maximum speed of the disk. At *N*=3 rpm the tip speed of the disk is about 0.07 m/s. As the minimum distance between the disk and the reactor wall or the scraper is 0.04 m, the shear rate can be estimated as $\frac{v_{\mathrm{tip}}}{\eta}=\frac{0.07\ \mathrm{m/s}}{0.04\ \mathrm{m}}\approx 1.8$ 1/s. The dynamic viscosity of the PC0210 liquid (Zhejiang Zhetiedafeng, China) was measured with a MARS40 Rheometer (Haake, Germany). When the shear rate ranges from 0.1~30 1/s, the apparent viscosity of PC0210 does not vary with the shear rate and thus the liquid exhibits Newtonian fluid properties in this range. Therefore, we use maltose solutions for our model experiments that do not involve chemical reactions. Mixtures of the highly viscous Newtonian liquid maltose (Hubei Qianxifeng, China) with water with viscosities in the range of 500 to 1200 Pa·s were used as the working fluid. Viscosities were measured using the MARS40 Rheometer at constant temperature 20 □, which is the experimental temperature as well. The maltose solutions density ranges from 1300 to 1400 kg/m^3, and surface tension of all maltose solutions is approximately 0.06 N/m.

3 Simulation

3.1 Volume of Fluid model (VOF)

Simulations on flows of multiphase Newtonian fluids are based on the solution of the continuity and Navier-Stokes equations. They are as follows:

$$\frac{\partial \rho}{\partial t}+\nabla\cdot(\rho \boldsymbol{v})=0 \tag{1}$$

$$\frac{\partial}{\partial t}(\rho \boldsymbol{v})+\nabla\cdot(\rho \boldsymbol{v}\boldsymbol{v})=-\nabla p+\nabla\cdot[\mu(\nabla \boldsymbol{v}+\nabla \boldsymbol{v}^T)]+\rho \boldsymbol{g}+\boldsymbol{F} \tag{2}$$

where t is time, $\boldsymbol{v}$ is the velocity vector, p is the pressure, $\boldsymbol{g}$ is the gravitational acceleration vector, μ is the viscosity, ρ is the density, and $\boldsymbol{F}$ is the body force.

A Volume of Fluid (VOF) model (Hirt and Nichols, 1981) was employed for simulating the laminar, incompressible, and isothermal film flow. The effective viscosity and density are defined as the volume-fraction-averaged parameters μ and ρ. They are as follows:

$$\rho=\rho_{\mathrm{l}}\alpha_{\mathrm{l}}+\rho_{\mathrm{g}}\alpha_{\mathrm{g}} \tag{3}$$

$$\mu=\mu_{\mathrm{l}}\alpha_{\mathrm{l}}+\mu_{\mathrm{g}}\alpha_{\mathrm{g}} \tag{4}$$

where the α is the volume fraction of different phases. The subscript g refers to the gas phase and l to the liquid phase. The volume fraction is limited by the following equation:

$$\alpha_l + \alpha_g = 1 \tag{5}$$

The effect of surface tension is transformed into a body force and added as a source term in the Navier-Stokes equations (Brackbill et al., 1992). The body force $\boldsymbol{F}$ between the two phases is expressed by:

$$\boldsymbol{F} = \sigma \frac{\rho \kappa \nabla \alpha_l}{\frac{1}{2}(\rho_l + \rho_g)} \tag{6}$$

where σ is the surface tension and κ the gas-liquid interface curvature defined in terms of the divergence of the unit normal vector:

$$\kappa = -\nabla \cdot \hat{\boldsymbol{n}} \tag{7}$$

where

$$\hat{\boldsymbol{n}} = \frac{\boldsymbol{n}}{|\boldsymbol{n}|} \tag{8}$$

$$\boldsymbol{n} = \nabla \alpha_l \tag{9}$$

3.2 Numerical details

The geometric configuration used for the CFD simulations in this work was the same as that for the experiments. A spoked disk was mounted on a shaft. Structured hexahedral cells were generated by using the commercial software ICEM, shown in Fig. 2. The total number of elements used in CFD modeling was 3,581,950. To accurately calculate the film flow, a boundary layer mesh was employed near the spoked disk. In order to determine the necessary mesh size to provide an adequate representation of the film flow, the experimental film thickness results were used as a guideline. The minimum experimental thickness was about 5 mm. In the thickness direction (axial direction), a mesh size of 1 mm was maintained near the disk surface so as to yield at least 5 cells within the film. The mesh size of the edges in other areas varied from 3 mm to 4.5 mm. Miah et al. adopted a similar grid generation strategy (Miah et al., 2016; Miah et al., 2017). We have carried out exhaustive grid independence studies and found this strategy is sufficiently refined to capture the flow details, with Fig. 2(c) showing evidence of this.

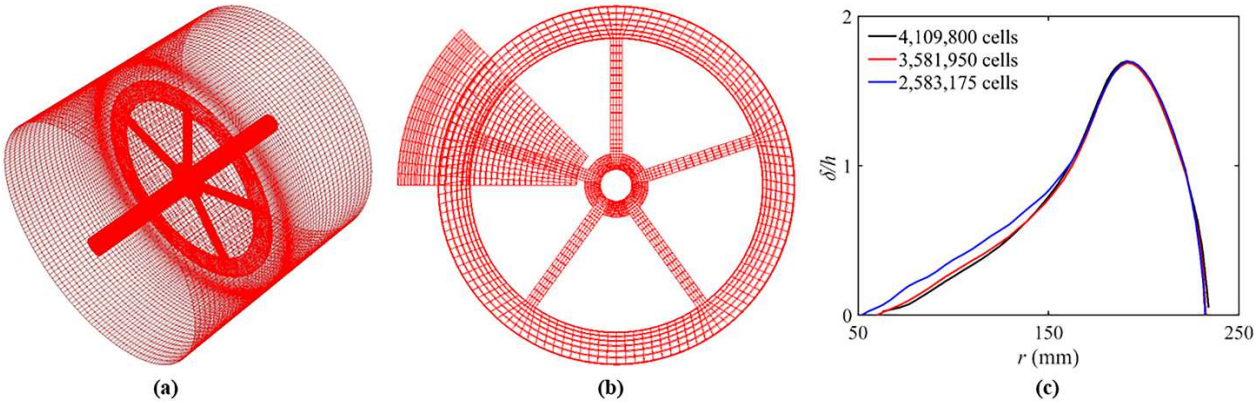

Fig. 2 - The structured hexahedral mesh for the numerical calculation model. (a) The grid except for the scraper; (b) The position and surface grid of the scraper and rotor; (c) Dimensionless film thickness in radial direction after half a revolution at θ=90 °, N=3 rpm,

μ=700 Pa·s and H=0.4T.

Transient simulations for the film formation process were carried out using Ansys Fluent 2020R1. As for the temporal resolution, for a minimum mesh size of 0.25 mm (this minimum mesh size was applied in the radial direction where the disk meets the shaft) and different angular velocity, the time step was set as 0.001~0.0001 s to keep the Courant-Friedrichs-Levy number smaller than 1 (Ferziger and Peric, 2002). The no-slip condition was applied to all solid wall boundaries. The walls at the left and right ends of the reactor were set as symmetry boundary conditions. The surface tension of the liquid against air is set to 0.059 N/m. The contact angle is set to 30^{o}. The spoked disk motion was simulated using the sliding mesh approach according to ANSYS Fluent Users guide (ANSYS Inc., 2020). The second-order upwind scheme was used for the spatial discretization of the momentum equations, and the implicit scheme for volume fraction parameters. In order to couple pressure and velocity, the SIMPLE (Semi-Implicit Method for Pressure Linked Equations) algorithm was used. The density of air was 1.225 kg/m^3 and the viscosity was 1.789×10^{-5} Pa·s. The properties of the liquid will be indicated later.

4 Results and discussion

4.1 Film formation

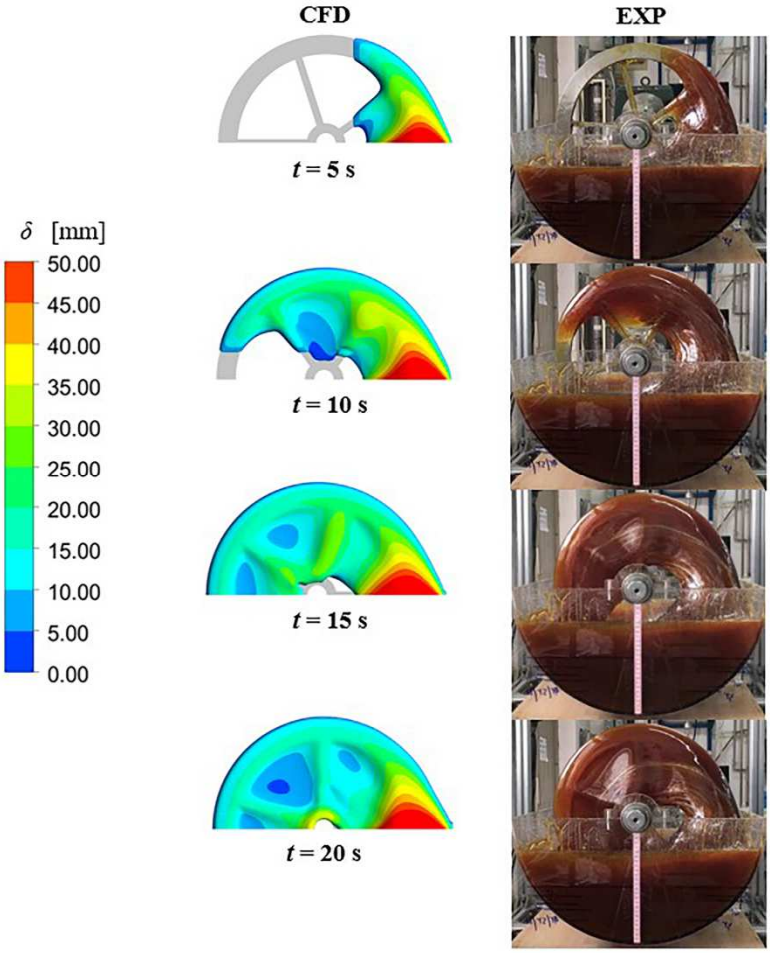

Fig. 3 – The simulated (left) and experimental (right) process of film formation as a function of time. The operation condition is N=3 rpm, μ=700 Pa·s and H=0.4T.

Previous studies have defined two types of film according to the film formation, which are a bounded film and an unbounded film. The former is attached to the solid wall with one gas-liquid interface, the latter is flowing without the support and has two gas-liquid interfaces. Both of them can be seen on a spoked disk (Cheng et al., 2018; Takamasa and Kobayashi, 2000).

Fig. 3 shows the experimental and simulated film formation process on the spoked disk at different moments in time, where t=0 is defined as the moment the disk starts spinning. This configuration does not contain a scraper. We see that the time evolution of film formation in the simulation closely follows that in the experiment. In general, the film is thickest where the spoked disk surface emerges from the liquid bath. It gradually becomes thinner and fluctuates due to the alternation of ring, spoke, and open window zones. The film inside the open window region tends to be thinner. We note here that film thickness δ is defined as the maximum distance from the liquid molecules in the film to the gas-liquid interface. The effect of thinning of the film inside the windows is weaker compared to previous research (Cheng et al., 2018; Deng and Dai, 2015b; Miah et al., 2017). This is due to the much higher viscosity of the liquid used in the current study. The unbounded film in the first window (along the rotation direction) is much thicker than in the later windows, which may be a direction to intensify transfer processes for polymer devolatilization. In section 4.5 of this article, we will set a scraper to reduce the film thickness in an attempt to enhance surface renewal.

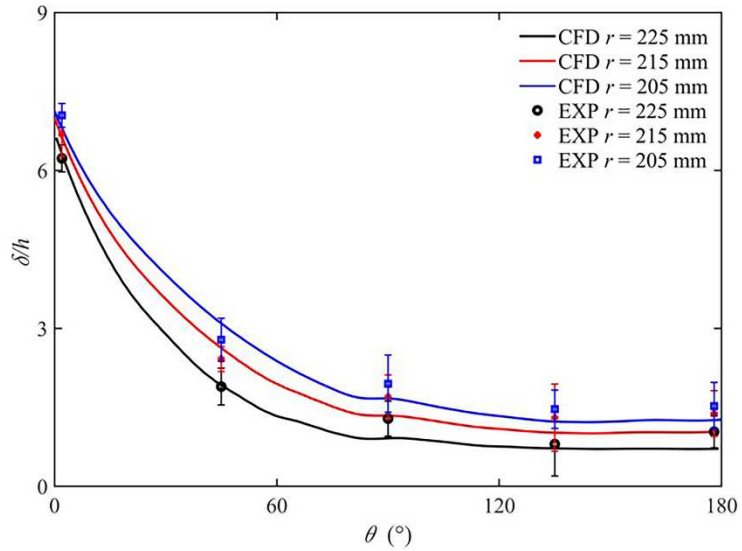

Fig. 4 - The experimental and simulated dimensionless film thickness with angular coordinate after the disk has completed one full revolution. The operation condition is N=3 rpm, μ=700 Pa·s and H=T/3. An error bar represents one standard deviation.

The geometric configuration applied for the CFD simulations in this work was the same as that used for the experiments. We have defined the dimensionless film thickness as $\frac{\delta}{h}$ with h=10 mm the thickness of the disk. The comparison between experimental and simulated dimensionless film

thickness is shown in Fig. 4. It can be seen that the CFD simulated results agree well with the experimental data, following the same trend as the experiments with respect to the angular location (θ) as well as the radial location (*r*) on the disk.

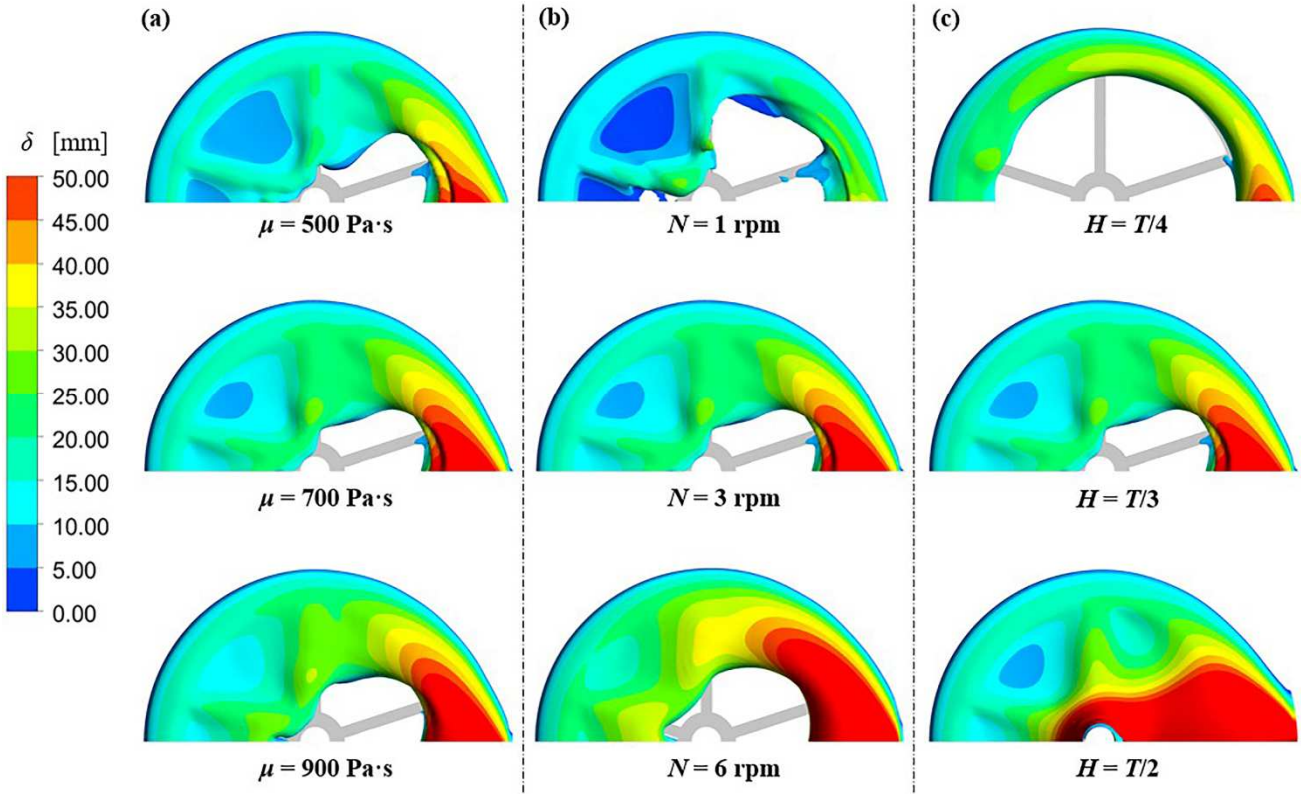

Fig. 5 - The simulated distribution of film thickness in different operation condition calculated after the disk has completed one full revolution. (a) The distribution of film thickness as a function of viscosity and the operation condition is *N*=3 rpm and *H*=*T*/3; (b) The distribution as a function of rotating speed and the operation condition is *μ*=700 Pa·s and *H*=*T*/3; (c) The distribution as a function of liquids level and the operation condition is *N*=3 rpm and *μ*=700 Pa·s.

As shown in Fig. 5, in super-high-viscosity liquid, the film thickness increases with decreasing radial position due to gravity, which drags the liquid film down. At the same time, the film is difficult to cover the surface of the plate due to its poor fluidity. The viscous force and gravity force are more important than the inertial force. This was different in previous studies that had higher rotational speeds of the disk and lower viscosities (Cheng et al., 2018; Vijayraghvan and Gupta, 1982).

In Fig. 5(a), the liquid coverage of the spoked disk decreases, and the film thickness increases as the viscosity increases. Both effects increase mass transfer resistance. In Fig. 5(b), increasing the disk speed results in a thicker film on the solid surface of the wheel. The film has less time to be drained down by gravity and – as a result – the windows remain more open when the rotational speed increases from 3 to 6 rpm. The more open window at 1 rpm was formed because part of the film has drained down to the tank as it has sufficient time for falling. These observations agree with those of Miah et al. (2016) and Vijayraghvan and Gupta (1982) who concluded that viscosity and rotating speed are the main factors for the film formation in the single-shaft rotating disk reactor.

In addition, we find that the liquid level has a significant influence on film formation, especially for highly viscous liquids, see Fig. 5(c). The area and the thickness of film increase with liquid height inside the reactor. In a significant portion of the cases shown in Fig. 5, the liquid only partly covers the disk, specifically for θ between 0° to 90°. Cases that have significant coverage of liquid on the disk suffer from relatively thick films at small angles θ resulting in poor mass transfer. Later in the paper, we will show that a scraper is able to mitigate this issue.

4.2 Dimensional analysis

In order to place the results of experiments and simulations on film formation into context as well as to identify the essential physics of this wetting problem, we here provide a brief dimensional analysis. The process deals with the following five physical effects: gravity, viscous effects, surface tension, wetting (i.e. contact angle), and inertia. There are two fluids involved: a very viscous Newtonian liquid and air.

Given the relatively low density and viscosity of air as compared to the liquid, air plays only a marginal role. The airflow driven by the rotating disk is very weak and will be hard to distinguish from other auxiliary effects such as free convection due to slight temperature differences. At N=3 rpm the tip speed of the disk is about 70 mm/s. The speed of a free convection airflow with as a vertical length scale the diameter D of the disk can be estimated as $\sqrt{g\Delta\rho D/\rho}$. In order to achieve a free convection flow with the same speed as the tip speed of the disk, we only need $\Delta\rho/\rho \approx 10^{-3}$ which translates to about 0.3 ^{o}C temperature difference. This means that very slight variations in surroundings will influence the airflow as much as the spinning wheel but will have hardly any impact on the behavior of the highly viscous liquid. We thus are allowed to base dimensionless numbers on the liquid properties.

Effects of liquid inertia – as compared to viscous effects – are marginal. If we define Reynolds $\mathrm{Re} = \frac{\rho v_{\mathrm{tip}} D}{\mu}$, it has a value of $\mathrm{Re} \approx 0.07$. At the same time, effect of surface tension as compared to viscous effects is marginal. If we define a capillary number as $\mathrm{Ca} = \frac{\mu v_{\mathrm{tip}}}{\sigma} \approx 10^{3}$. Given the weak effect of surface tension, we also expect minor effects of the contact angle of the liquid on the surface of the wheel.

The film formation process therefore is governed by a competition between gravity and viscosity. This allows us to come up with a crude estimate of the expected film thickness: we expect the dimensionless number $\frac{\rho g \delta^2}{\mu v_{\mathrm{tip}}}$ to be order one. As a result, $\delta = \sqrt{\frac{\mu v_{\mathrm{tip}}}{\rho g}} \approx 60$ mm which – given the experimental results as e.g. presented in Fig. 4 – is the correct order of magnitude.

4.3 Flow fields

Fig. 6 shows two liquid circulations on the surface of the liquid bath located on either side of the disk. The circulations are caused by the competition between gravity and viscous forces. Part of the liquid makes a full circulation on the disk (from point A to B to C and again to point A). Around point B a significant portion of the liquid is dragged down by gravity back into the bath where it then moves to point D and then to point A. This recirculation of liquid in the bath is also clearly visible in Fig. 6(b).

The velocity field can be divided into three zones on the surface of the circular disk: the initial zone, the accelerating zone, the steady flow zone, according to the relationship of velocity magnitude of the film with angular coordinate (Deng and Dai, 2015b), which is shown in Fig. 6(a).

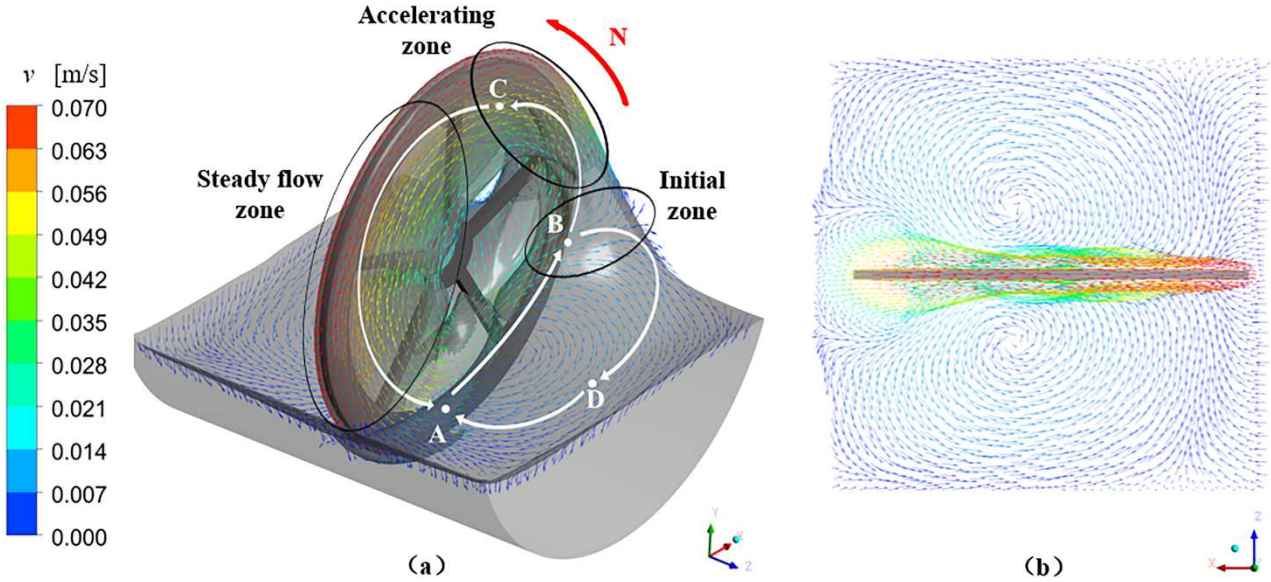

Fig. 6 – The velocity vectors on the film surface by simulation after the disk has completed one full revolution. (a) Axonometric drawing; (b) Top view. The operation condition is N=3 rpm, μ=700 Pa·s and H=T/3.

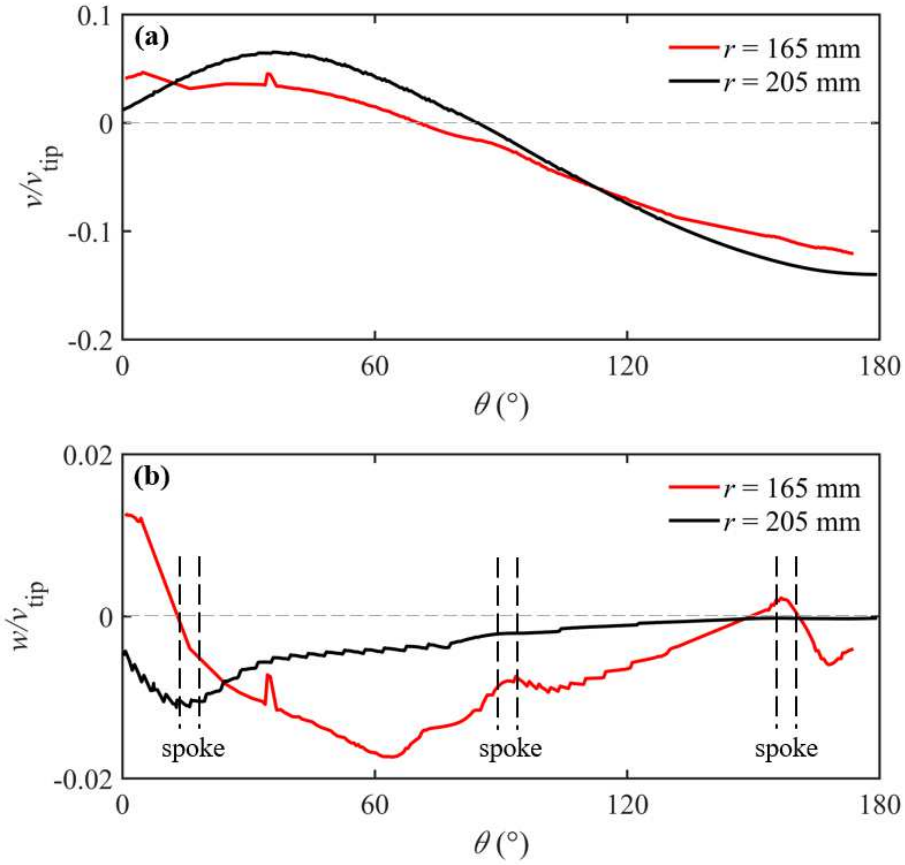

Fig. 7 - Dimensionless velocity on the surface of the film with angular coordinate after the disk

has completed one full revolution. (a) Dimensionless velocity in vertical (*y*) direction. (b) Dimensionless velocity in the direction normal to the disk (*z*-direction). The operation condition is *N*=3 rpm, μ=700 Pa·s and *H*=*T*/3.

Fig. 7(a) shows v/v_{tip}, dimensionless velocity in the *y* direction (vertical) on the film surface. Velocities are positive for θ up to 60^o with the liquid being drawn out of the tank. When θ is over 90°, v/v_{tip} gets negative, and the liquid film starts to fall back into the tank. The v/v_{tip} on the surface of the film in the open window (*r*=165 mm) is weaker than that in the film on the solid disk (*r*=205 mm).

Fig. 7(b) shows dimensionless velocity at the film surface in the *z* direction (axial). This is the direction normal to the disk with negative velocities being towards the disk. At *r*=165 mm velocities are mostly negative which means the film sinks into the open windows, leading to corrugation on the film. By comparing the velocity normal to the disk covering the windows (*r*=165 mm) and the solid region (*r*=205 mm) on the disk, it can be found that the normal velocity of the window area is greater.

4.4 Surface renewal

Danckwerts (1951) brought out the concept of surface renewal to describe transfer processes at gas-liquid interfaces. Later, Angelo et al. (1966) predicted rates of mass or heat transfer through stretching or shrinking phase boundaries of finite lifetime at low mass transfer rates, which is called the penetration theory for surface stretch. In addition, a new surface-renewal-stretch (SRS) model was developed by incorporating the previous two models (Jajuee et al., 2006). In the SRS model, the rate of fresh surface generation is used as the rate of surface renewal, which is defined as:

$$S = \frac{\partial A}{A \partial t} \tag{10}$$

where *A* is the film surface area. The surface renewal of the liquid film on the disk can be seen as the deformation of the liquid film on a two-dimensional plane (Deng and Dai, 2015a).

The linear deformation rate of the two-dimensional fluid element $\Delta x \Delta y$ in the *x* and *y* directions is

$$S_x = \frac{\partial u}{\partial x} \tag{11}$$

$$S_y = \frac{\partial v}{\partial y} \tag{12}$$

The relative deformation rate of a surface element $\Delta x \Delta y$ over time δt is

$$\frac{\Delta A}{A \delta t} = \frac{\left(\Delta x + \frac{\partial u}{\partial x}\delta x \delta t\right)\left(\Delta y + \frac{\partial v}{\partial y}\delta y \delta t\right) - \Delta x \Delta y}{\Delta x \Delta y \delta t} \tag{13}$$

By taking the limit of (Δx, Δy, δx, δy) to zero, this expression may be rewritten for any point on the interfacial surface as

$$\frac{\partial A}{A \partial t} = \frac{\partial u}{\partial x} + \frac{\partial v}{\partial y} \tag{14}$$

Combining Eq. (10) and Eq. (14), the rate of area deformation is given by:

$$S = \frac{\partial u}{\partial x} + \frac{\partial v}{\partial y} \tag{15}$$

When the density ρ is constant, the continuity equation for the incompressible fluid is defined

as follows:

$$\frac{\partial u}{\partial x}+\frac{\partial v}{\partial y}+\frac{\partial w}{\partial z}=0 \tag{16}$$

Therefore,

$$S=-\frac{\partial w}{\partial z} \tag{17}$$

The area average rate of film deformation S_{ave} can be calculated by the following equation:

$$S_{\text{ave}}=\frac{\iint_A\left(\frac{\partial u}{\partial x}+\frac{\partial v}{\partial y}\right)dxdy}{\iint_A dxdy} \tag{18}$$

It can be seen from Eq. (17) that stretching the surface area of the liquid film (S>0) is achieved by $\frac{\partial w}{\partial z}$<0. This implies $w\approx -Sz$ (Angelo et al. 1966) and therefore – in case of a stretching surface (S>0) – reduction of film thickness and exposure of liquid initially inside the film to gas.

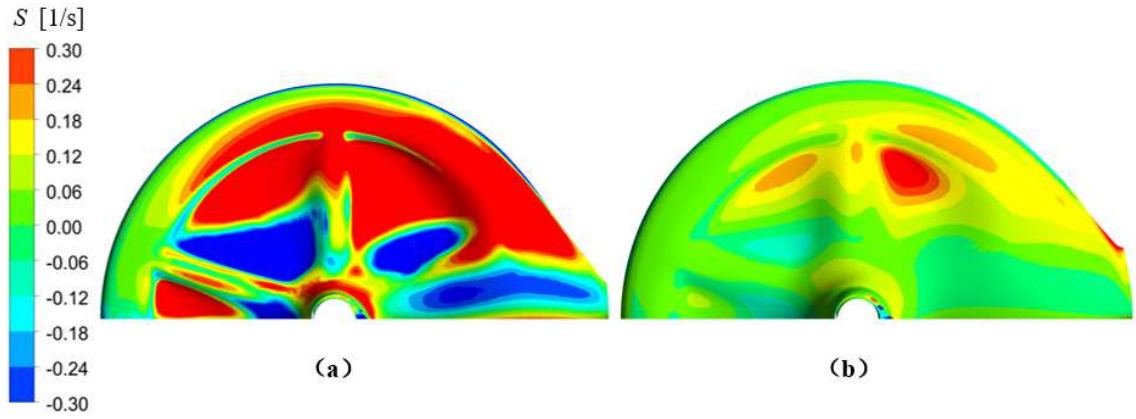

Fig. 8 - The simulated distribution of the film deformation rate. (a) N=10 rpm, μ=68 Pa·s, H=T/2; (b) N=3 rpm, μ=700 Pa·s, H=T/2.

The film distribution and deformation rate of the high-viscosity liquid (Fig. 8(a)) is different from those of the super-high-viscosity liquid (Fig. 8(b)). When operation conditions were set as N=3 rpm and H=T/2 for the high-viscosity liquid with μ=68 Pa·s, no continuous liquid film formed in the open windows, similar to the previous studies (Cheng et al., 2017, 2018). For the super-high-viscosity liquid with μ=700 Pa·s, the film spreads evenly in the open windows at N=3 rpm and H=T/2, as shown in Fig. 8(b). Thus, we select the two cases in Fig.8 for qualitative analysis.

In high-viscosity fluids shown in Fig. 8(a), the film thickness must decrease in the open windows due to the action of gravity draining out the film and the continuity requiring an increase of the velocity in the fluid falling direction, giving rise to a remarkable increase of the film deformation rate. In super-high-viscosity liquids, see Fig. 8(b), the effect of viscous force is dominating the competition between gravity and viscous force. It is much harder for the liquid to drain downward. The velocity gradient in the fluid falling direction decreases obviously and the surface renewal rate decreases significantly, as calculated with Eq. (15).

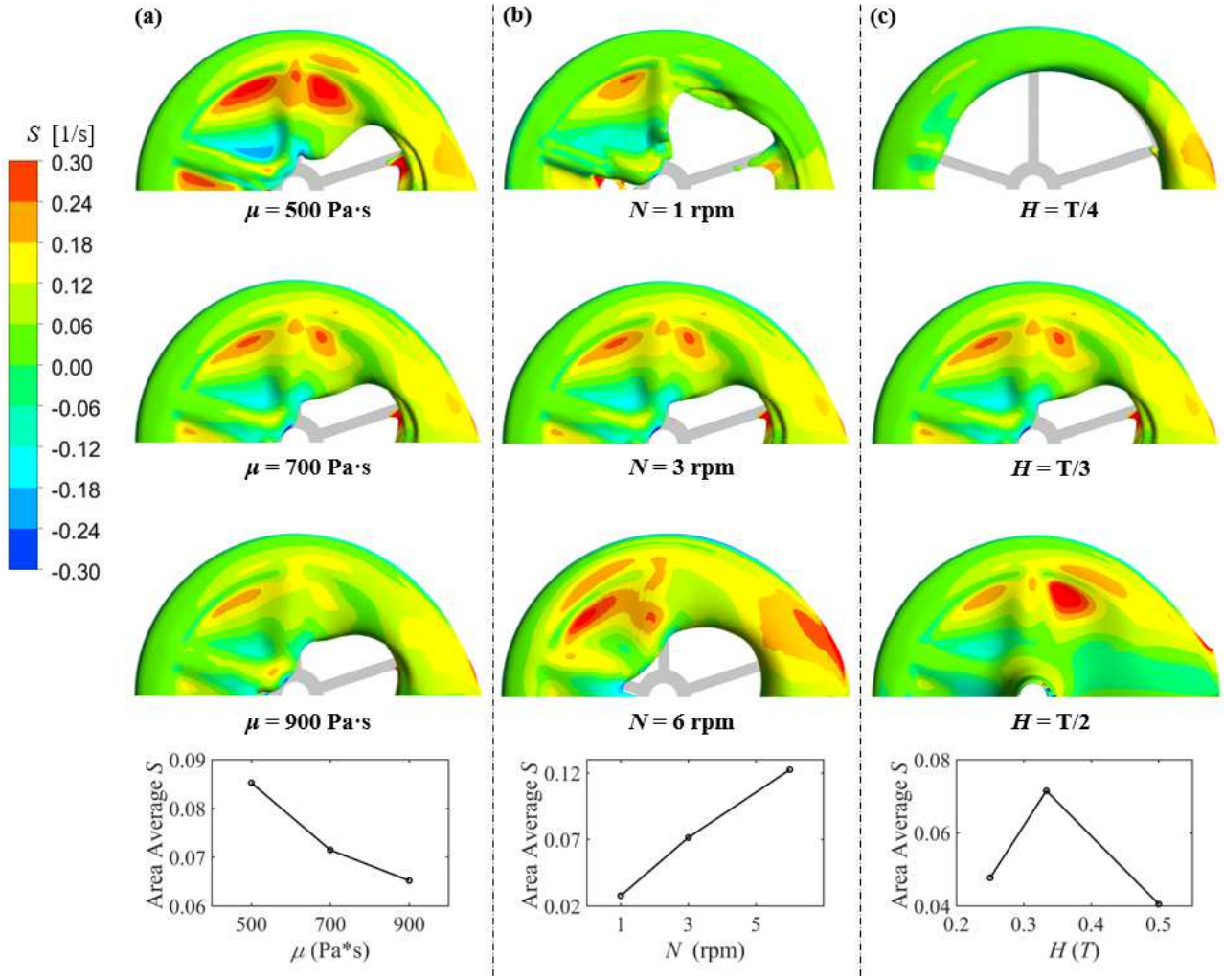

Fig. 9 - The simulated distribution of the film deformation rate under different operation condition after the disk has completed one full revolution. (a) The distribution for different viscosity at *N*=3 rpm and *H*=*T*/3; (b) The distribution for different rotational speed at μ=700 Pa·s and *H*=*T*/3; (c) The distribution with different liquids level at *N*=3 rpm and μ=700 Pa·s. The bottom row shows the area-average film deformation rate under different operation conditions.

Fig. 9 shows the distribution of the rate of film deformation in different operation conditions. Film on rotating disk becomes thicker when liquid viscosity increases and the mixing process is difficult, which makes the surface renewal worse. The area average rate of film deformation increases with the increasing rotating speed. However, as the rotational speed increases, the film-forming area on the disk decreases. Thus, the film formation area and film deformation rate need to be considered when setting the operating speed.

What is interesting is that the average rate of film deformation as a function of the liquid height is not monotonic and shows a maximum value, as shown in Fig. 9(c). In the industrial process, the liquid level is mostly set to 1/3 of the reactor diameter, which could be explained by the above result. Based on the above results, we can infer that in the actual production process, the operating conditions need to be adjusted according to the physical properties of the product to optimize the process.

4.5 Scraper design

The results of the previous sections demonstrate that there are options to intensify transfer processes for polymer devolatilization, especially for the super-high-viscosity liquid. In the final part of the paper, we are interested in the flow patterns that emerge when installing a scraper.

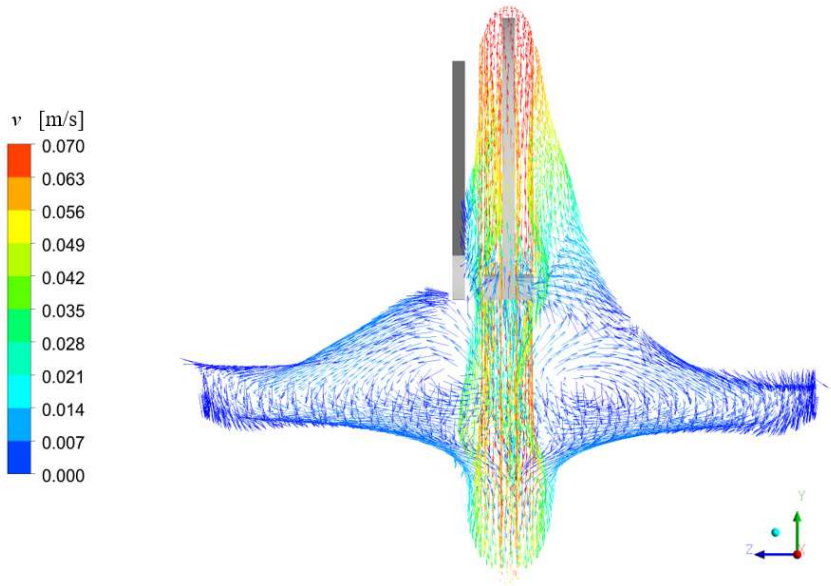

Fig. 10 - The simulated velocity vectors on the film surface in the reactor with a scraper (front view). The operation condition is *N*=3 rpm, *μ*=900 Pa·s and *H*=0.4*T*.

Fig. 10 reflects that the fluid being cut by the scraper loses its momentum and falls back into the reactor. The scraper can reduce the adhesion of the liquid phase during the devolatilization process, which reduces the film thickness and mass transfer resistance between the phases. In the meantime, the scraper pushes fluid to the other side of the disk, which may have a positive effect on the uniformity of the film thickness distribution on the other side.

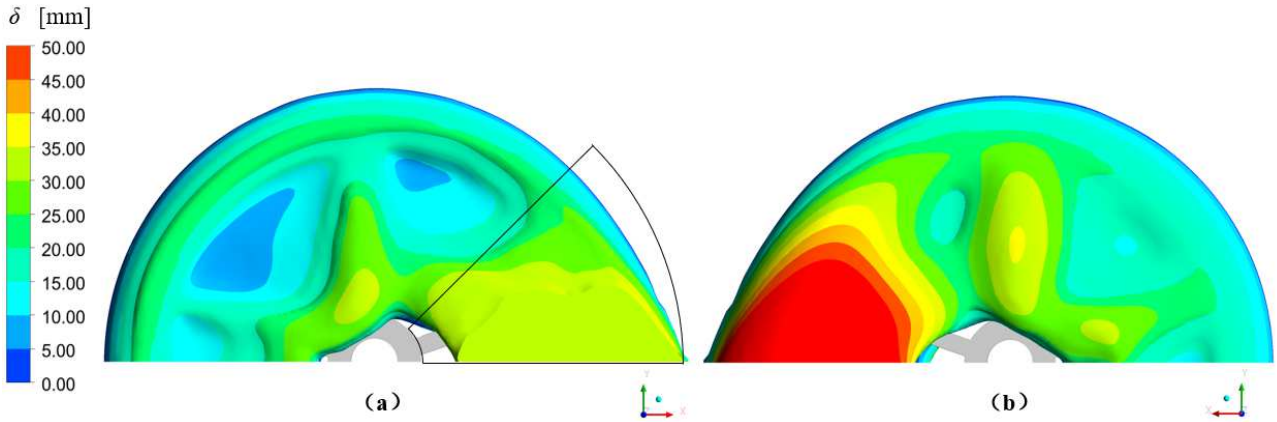

Fig. 11 - The simulated distribution of film thickness in the reactor with a scraper. (a) The scrape film. (b) The free film. The operation condition is *N*=3 rpm, *μ*=900 Pa·s and *H*=0.4*T*.

In Fig. 11 it is shown that there is a new type of film different from the free film. It is called the scrape film and exists in the region between scraper and disk. As for the scrape film, the film thickness is close to uniform and only slightly decreases in the both angular and radial direction. As the film thickness decreases, the resistance to the gas-liquid transfer process is reduced. Compared with Fig. 5, the scraper not only makes the scrape film spreads evenly on the disk but also the free film on the other side, which makes the area on the disk more effectively used.

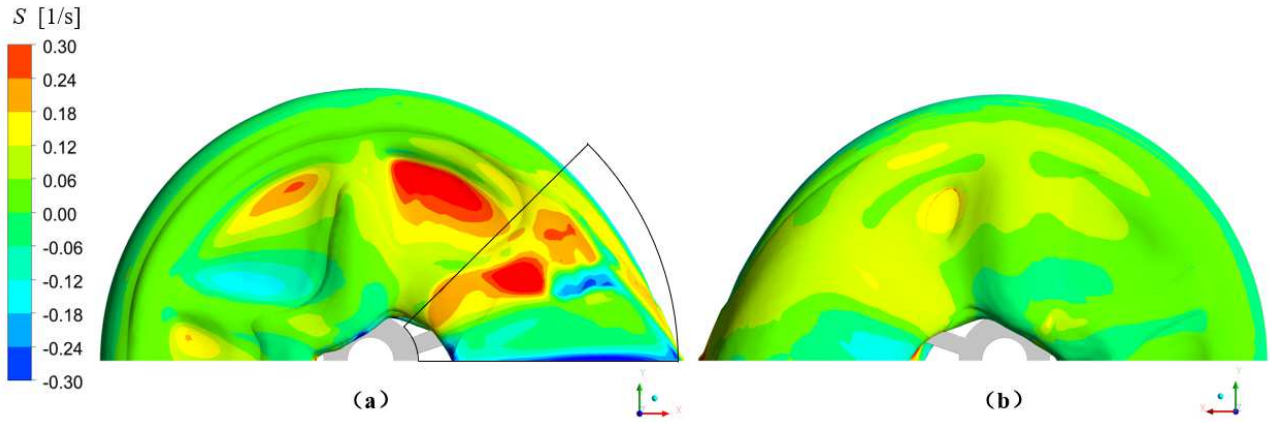

Fig. 12 - The simulated distribution of the film deformation rate in the reactor with a scraper. (a) The scrape film. (b) The free film. The operation condition is N=3 rpm, μ=900 Pa·s and H=0.4T.

Fig. 12 shows that the film deformation rate on the scraped film is much higher than the free film. It is because the scraper forcefully reduces film thickness and liquid phase adhesion. Combined with the previous analysis, the film deformation rate increases with the velocity normal to the flow direction. It is worth noting that, in the region where scraper and disk overlap, the film deformation rate is negative which demonstrates that the scraper has a squeezing effect.

5 Conclusion

The film formation and surface renewal of a highly viscous liquid on a rotating spoked disk were studied using experimental and CFD techniques. A simulation model was used including the Volume of Fluid model and sliding mesh method. For validation of the CFD predictions, the simulation results were compared to the experimental data and showed favorable agreement.

After studying the rheological properties. it was concluded that the PC melt is a highly viscous liquid that exhibits Newtonian characteristics at low shear rates. Therefore, we chose a maltose solution as the non-reacting experimental fluid.

For the film formation of super-high-viscosity liquid, the viscous force and gravity force are more important than the inertial force. In this paper, the film thickness increases with decreasing radial position due to gravity, which makes the liquid fall down. At the same time, the high viscosity makes it difficult for the liquid to cover the entire surface of the disk. For super-high-viscosity polymer devolatilization, the film formation and surface renewal need to be considered carefully when setting the operating speed and liquid height.

A scraper was designed to intensify transfer processes on the film of the super-high-viscosity.

Due to the cutting action of the scraper, the thickness of the scrape film is approximately uniform. Combined with the intensification of spoked windows, the film flow and surface renewal on the spoked disk are reinforced remarkably by the scraper.

Acknowledgements

The financial supports from the National Natural Science Foundation of China (No.21676007) are gratefully acknowledged.

Reference

Afanasiev, K., Münch, A., Wagner, B., 2008. Thin film dynamics on a vertically rotating disk partially immersed in a liquid bath. Applied Mathematical Modelling 32, 1894-1911.

Angelo, J.B., Lightfoot, E.N., Howard, D.W., 1966. Generalization of the penetration theory for surface stretch: Application to forming and oscillating drops. AIChE Journal 12, 751-760.

ANSYS Fluent User Guide, ANSYS Inc., 2020.

Brackbill, J.U., Kothe, D.B., Zemach, C., 1992. A continuum method for modeling surface tension. Journal of Computational Physics 100, 335-354.

Cheng, W., Wang, J., Gu, X., Feng, L., 2017. Film formation in a horizontal twin-shaft rotating disk reactor for polymer devolatilization. Chemical Engineering Science 166, 19-27.

Cheng, W., Wang, J., Gu, X., Feng, L., 2018. Film flow on rotating wheel in a horizontal twin-shaft reactor for polymer devolatilization. Chemical Engineering Science 191, 468-478.

Cheong, S.I., Choi, K.Y., 1995. A study on the polymer layer-forming phenomena in a rotating disk polycondensation reactor. Journal of Applied Polymer Science 55, 1819-1826.

Coughlin, R.W., Canevari, G.P., 1969. Drying polymers during screw extrusion. AIChE Journal 15, 560-564.

Danckwerts, P.V., 1951. Significance of liquid-film coefficients in gas absorption. Industrial & Engineering Chemistry 43, 1460-1467.

Deng, B., Dai, G., 2015a. Numerical simulation of surface renewal frequency on vertically rotating disc. CIESC Journal (Chinese) 66, 1407-1416.

Deng, B., Dai, G., 2015b. Simulation of the flow field of a vertically rotating disc reactor. Chemical Reaction Engineering and Technology (Chinese) 31, 254–261.

Dwyer-Joyce, R.S., Drinkwater, B.W., Donohoe, C.J., 2003. The measurement of

lubricant-film thickness using ultrasound. Proceedings of The Royal Society A: Mathematical, Physical and Engineering Sciences 459, 957-976.

Ferziger, J.H., Peric, M., 2002. Computational Methods for Fluid Dynamics. Sprigner.

Finkeldei, F.W.F., 2003. Batch polycondensation method and a rotating disc reactor therefore, US Patent 20030139543A1.

Ganguly, A., Channe, P., Jha, R., Mitra, S., Saha, S., 2021. Review on transesterification in polycarbonate–poly (butylene terephthalate) blend. Polymer Engineering & Science 61, 650-661.

Hasan, N., Naser, J., 2009. Determining the thickness of liquid film in laminar condition on a rotating drum surface using CFD. Chemical Engineering Science 64, 919-924.

Hirt, C.W., Nichols, B.D., 1981. Volume of fluid (VOF) method for the dynamics of Free Boundaries. Journal of Computational Physics 39, 201-225.

Hu, J., Yang, X., Yu, J., Dai, G., 2016. Numerical investigation on hydrodynamics of vertically confined free film. Canadian Journal of Chemical Engineering 94, 340-348.

Hu, J., Yang, X., Yu, J., Dai, G., 2017. Carbon dioxide (CO2) absorption and interfacial mass transfer across vertically confined free liquid film-a numerical investigation. Chemical Engineering and Processing 111, 46-56.

Jajuee, B., Margaritis, A., Karamanev, D., Bergougnou, M.A., 2006. Application of surface-renewal-stretch model for interface mass transfer. Chemical Engineering Science 61, 3917-3929.

Hanimann, K., Stibal, W., 2013. Method and device for producing polyester granules and/or shaped parts with a low acetaldehyde content, US Patent 8470220.

Miah, M.S., Al-Assaf, S., Yang, X., McMillan, A., 2016. Thin film flow on a vertically rotating disc of finite thickness partially immersed in a highly viscous liquid. Chemical Engineering Science 143, 226-239.

Miah, M.S., Hossain, M.S., Ashraf, M.A., Al-Assaf, S., McMillan, A., 2017. Numerical simulation of non-Newtonian polymer film flow on a rotating spoked annulus. Journal of Applied Polymer Science 134, 44943.

Palmer, D., 2000. Mixing kneader, US Patent 6039469.

Sebastian, D.H., Biesenberger, J., 1983. Principles of polymerization engineering. Wiley.

Takamasa, T., Kobayashi, K., 2000. Measuring interfacial waves on film flowing down tube

inner wall using laser focus displacement meter. International Journal of Multiphase Flow 26, 1493-1507.

Uwe Stueven, B.S.D., Leo Van Miert, A.B., Dominicus van Esbroeck, A.N., Oskar Stephan, H.D., Annemarie Hillebrecht, M.D., Huanmin Wei, F.D., 2011. Mixing kneader and process for preparing poly(meth)acrylates using the mixing kneader, US Patent 8070351.

Vijayraghvan, K., Gupta, J.P., 1982. Thickness of the film formed on a vertically rotating disk partially immersed in a Newtonian liquid. Industrial & Engineering Chemistry Fundamentals 21, 333-336.

Xie, H., Hu, J., Dai, G., 2018. Numerical simulation on flow behavior of twin‐liquid films over a vertical plate with an open window. AIChE Journal 64, 1458-1468.